nature communications

Article

https://doi.org/10.1038/s41467-025-66082-3

Fluorine-free binder-based dry thick electrodes with Parafilm® M toward sustainable and efficient battery manufacturing

Received: 4 February 2025

Accepted: 29 October 2025

Published online: 16 December 2025

Check for updates

Min Kyung Kim[1,2,3,17], Taegyun Yu[1,17], Sungbin Jang[1,4,17], Juho Lee[1,3,5], Hyeseong Oh[5], Min Jang[1,5], Hyungyeon Cha[1], Huiyeol Lee[2], Joonhee Kang[2], Seung Min Lee[1,5], Hyeongseok Shim[1], Kwon-Hyung Lee[1], Gyujin Song[1], Wooyoung Jin[1], Tae-Hee Kim[1,6], Sinho Choi[1], Kyeong-Min Jeong[5], Joong Tark Han[7,8], Jung-Keun Yoo[9], Hun-Gi Jung[9,10,11,12], Sanghyun Song[13], Myoungkeon Park[13], Jinwoo Seong[13], Dongoh Kim[13], Hyunwoo Choi[14], Minjong Seong[14], Min Jin Lim[14], Wook Ryol Hwang[14,15], Jieun Nam[16], Sanghoon Jo[16] & Jinsoo Kim[1,3]

Dry electrodes are being actively developed for sustainable and efficient battery manufacturing. Currently, polytetrafluoroethylene binders dominate dry processes, raising concerns about high fluorine content regarding restrictions on per- and polyfluoroalkyl substances. Moreover, the poor adhesion necessitates a wet coating-based primer layer, which dilutes its main objectives. Here, we show dry processing approach using a thermoplastic, fluorine-free binder with low environmental impact and high productivity. Parafilm® M, a laboratory sealing film formulated with low-cost paraffin and polyethylene, consists of saturated linear hydrocarbons, offering high chemical stability from strong C-H covalent bonds and a large highest occupied molecular orbital - lowest unoccupied molecular orbital energy gap. It also has a low glass transition temperature, enabling mild-pressure activation to interconnect active materials while achieving true solvent-free adhesion without the wet-coating of primers on the current collector. This dry electrode binder provides substantial electrochemical properties based on $LiNi_{0.8}Co_{0.1}Mn_{0.1}O_2$ positive electrode over 5 mAh cm^{-2} for 600 cycles. This integrated approach bridges the gap between materials and processes, paving the way for sustainable advancements in battery electrode manufacturing.

The ever-growing demands for high-performance lithium-ion batteries (LIBs) have pushed forward advanced developments in electrode manufacturing processes to improve efficiency while reducing environmental impacts[1,2]. Traditionally, wet processes have been the primary methods for fabricating electrodes based on the slurry casting technique. However, these methodologies have serious drawbacks, both high capital expenditures (CAPEX) and operational expenditure (OPEX) for the extensive solvent drying, as well as carbon dioxide

A full list of affiliations appears at the end of the paper. e-mail: jinsoo.kim@dgist.ac.kr

(CO_2) emissions in terms of high energy utilization and the exhausted solvent as a carbon source[3,4]. The wet process is also incompatible to coat high-loading thick electrodes because of carbon-binder domain (CBD) migration during the solvent transport, which hindered the high-energy-density batteries[5,6]. In this context, dry electrode fabrication offers a promising compromise for more sustainable and low cost production of LIBs[7–17].

Dry electrode manufacturing primarily depends on polytetrafluoroethylene (PTFE) binders due to high chemical stability and fibrilizing properties under high shear conditions[7,9,18]. Besides all these advantages, PTFE binders are linked with several environmental issues[19,20]. PTFE is produced with a considerable level of CO_2 emission, and its byproduct is associated with high global warming potential (GWP), meaning that PTFE emits a severe carbon footprint that dilutes the core value of the dry electrodes[21–23]. In addition, PTFE is a representative fully fluorinated chemical species, so the recent trend to restrict per- and polyfluoroalkyl substances (PFAS) casts doubt on its use[24–26]. Such concerns drive the need for alternative fluorine-free binders that can sustain the mechanical integrity and electrochemical performance of dry electrodes.

In addition to environmental issues, the adhesion of dry electrodes to current collectors is controversial because PTFE has a non-sticky nature[27–29]. For that reason, an adhesive primer layer, mainly composed of carbon black as well as aqueous binders such as styrene butadiene rubber (SBR) and carboxymethyl cellulose (CMC), with a wet process has to be applied before the coating process with dry electrodes[30,31]. This is paradoxical to the solvent-free manufacturing of dry electrodes, thus making it difficult to achieve the intended benefits for the environmentally friendly process. PTFE is also hydrophobic, so the dry electrodes might not be well-immersed in the liquid electrolyte, especially with the high loading, high density, and large area. PTFE is also known to be irreversibly reduced with lithium ions below 1 V vs. Li^+/Li, which is problematic for dry negative electrodes[14,31–35]. From the viewpoint of process development, the PTFE-based freestanding dry electrodes can have issues with the high-tensioned roll-to-roll manufacturing due to the low mechanical strength[36,37]. These result in the necessity of developing alternative binders and improved processing concepts that implement genuine dry electrode manufacturing with improved processibility.

This study presented a distinctive approach to dry electrode manufacturing using a thermoplastic fluorine-free binder, which is Parafilm® M (hereafter Parafilm). This is widely used as laboratory sealing film and comprises mostly saturated hydrocarbon chemical species, primarily known as paraffin and polyethylene (PE), with C-H and C-C covalent bonds, as the molecular weight analysis in shown in Supplementary Fig. 1. It has relatively low CO_2 emission, GWP impact, and cost compared to PTFE[38]. It also gives chemical and electrochemical stabilities owing to the robust molecular structure. Parafilm is also sticky and has a glass transition temperature (T_g) around 60 °C, which can enable the low-energy processing concept. Combining those properties provides facile activation for enhanced processibility through cold or warm pressing methods.

The only previous trial to use paraffin as an electrode binder was carried out by Passerini et al., which previously investigated thick electrodes using a blend of paraffin wax, polypropylene, and stearic acid as a sacrificial softening agent by debinding thermal treatment[39]. The electrodes contained 55 vol% of active materials and were produced via twin-screw extrusion. In contrast, our study adopts a more streamlined approach, utilizing Parafilm as the primary binder with 1 ~ 2 wt% of composition and simplifying the overall electrode fabrication process. Our work showed that the Parafilm-based binders offer a promising solution to achieve dry thick electrodes with high specific areal capacities over 5 ~ 9 mAh cm^{-2} for $LiNi_{0.8}Co_{0.1}Mn_{0.1}O_2$ (NCM811) positive electrodes, which operated for over 1000 cycles. This chemical species enables primer-free adhesion to current collectors. The dry-mixed powder exhibits a granulated morphology, in contrast to the massive compound typically seen in PTFE-based composites. Such morphology facilitates potential application in conventional pattern-coated electrode designs through controlled powder feeding. All these inherent features in Parafilm reduce the environmental impact of LIB production, improving the practical aspect and the scalability of dry electrode fabrication. This alternative strategy with improved binder chemistry paves the way toward absolute dry electrodes for sustainable and efficient battery manufacturing.

Results and discussion

Environmental and economic impacts of representative electrode binder chemistries

Binder chemistries are critical for sustainable and efficient battery electrode manufacturing. They influence both environmental impact and processibility. Figure 1 shows a detailed comparison of structural, economic, and environmental attributes regarding the choice between structurally identical but chemically differed PTFE, polyvinylidene fluoride (PVDF), and Parafilm binders and their implications for electrode manufacturing. Figure 1a–c gives the structural comparison between the repeating units of those binders. PTFE is a linear, fully fluorinated polymer and chemically inert. Because of this property, it is one of the most common polymers in dry electrode processes. In contrast, PVDF is a half-defluorinated and protonated polymer widely used in wet electrode processes. Parafilm has a fully defluorinated and protonated linear carbon chain with the same backbone as PTFE and PVDF. Such a stepwise variation, starting from PTFE and going through to Parafilm, strongly supports the transitioning of binder chemistries toward lower environmental impact.

Economic considerations are a significant feature in determining the feasibility of emerging compounds for large-scale applications. Figure 1d compares the expenses related to PTFE, PVDF, and Parafilm. Though quite effective, PTFE is the most expensive choice, which is an important drawback for cost-effective manufacturing. PVDF is the moderate choice in expense, but it still faces quite notable expenses. Parafilm is the most cost-effective binder, helping reduce material expenses by almost 1/23 compared to PTFE. This economic benefit of Parafilm makes it a feasible replacement for conventional binders used in dry electrode processes. Furthermore, as the transition from wet to dry processing becomes increasingly necessary for sustainable battery manufacturing, Parafilm offers an optimized solution by broadening the binder selection available for dry processes and supporting scalable, environmentally friendly fabrication.

One of the major concerns for greener manufacturing is the environmental impact of binder materials. The GWP of PTFE, PVDF, and Parafilm was rated as presented in Fig. 1e. PTFE has the highest GWP because, during its production process, it emits potent greenhouse gases such as perfluoroethane (PFC-116). Even with a partially reduced fluorine content, PVDF contributed to high GWP with compounds such as 1,1,1-trifluoroethane (HFC-143a)[22]. On the other hand, Parafilm, containing paraffin and PE, has the lowest GWP, thus offering a favorable environmental benefit. This considerable peaking reduction in GWP from PTFE to Parafilm makes a strong point about the potential use of Parafilm as a binder for substantial environmental improvements in LIB manufacturing. Based on this analysis, PTFE has several concerns that can dilute the core intentions regarding the environmental and economic objectives of dry electrode processing. However, Parafilm shows strong benefits owing to its low cost and environmental aspect, which can be an alternative to PTFE as a dry electrode binder.

Figure 1f presents the advantages of Parafilm in a simplified dry electrode fabrication process compared with PTFE, which requires an additional primer layer for mechanically weak freestanding electrodes to adhere to current collectors. Parafilm provides natural adhesion without an additional primer coating, and dry mixed powder can be

directly applied onto current collector and pressed into electrodes. Furthermore, the dry mixed granulated composite with Parafilm binder is feasible for controlled feeding powders that can be pattern-coated to the electrodes, which is not possible to implement with PTFE-based freestanding dry electrodes. The inset shows our proof-of-concept experiments in lab-scale further to prove the Parafilm-based dry electrode processing concept for practicality.

Chemical and thermal properties of representative binders

Moreover, the need to replace PTFE with Parafilm as a dry electrode binder is further substantiated by its relevant chemical stability and thermal properties for efficient battery manufacturing. These are presented in Fig. 2, indicating the advantages of Parafilm compared with traditional binders like PTFE and PVDF. Figure 2a and Supplementary Table 1 compare the Fourier transform infrared spectroscopy (FTIR) spectra of PTFE, PVDF, and Parafilm to observe their local chemistries. The most primary peaks in the FTIR spectrum come in absorption band at 612 cm^{-1} (-CF_2), 1175 cm^{-1} (-CF), and 1213 cm^{-1} (-CF_3) in PTFE and PVDF, which indicates that these polymers are fluorine-rich. The spectrum of PVDF is similar to PTFE, but it has a C-H peak at 1396 cm^{-1} and lacks a CF_3 peak[40]. In contrast, Parafilm does not indicate any signal corresponding to a C-F bond, definitely establishing its fully defluorinated, totally protonated nature. Parafilm exhibits various peaks at 1396 cm^{-1} for CH, 1468 cm^{-1} for CH_3, and CH_2 stretching between 2840 ~ 2960 cm^{-1}. At the FTIR peaks, we can infer that the structural composition of paraffin and PE[41]. The transition from PTFE to Parafilm involves defluorination of the carbon backbone, resulting in a fluorine-free binder. In other words, Parafilm has a structurally identical linear carbon chain of the polymer as PTFE but with differently terminated fluorine or proton. The absence of fluorine makes it less hazardous to the environment, thus making Parafilm more appropriate as a relatively sustainable dry electrode binder for LIBs.

Thermal properties are significant to polymers, especially the T_g, when choosing binder materials since they define the activations during processing. Figure 2b presents differential scanning calorimetry (DSC) data for PTFE, PVDF, and Parafilm. The DSC curves show that Parafilm exhibits a facile thermoplastic behavior compared to PTFE and PVDF at about 60 °C. The other minor heat releasing peaks for the Parafilm were observed at 45 °C and 99 °C. The PTFE binder has a minor exothermic peak at 20 °C and a main peak at 327 °C. The PVDF peaks well-match with the literature, observed at 171 °C. Therefore, this low T_g implies that low-energy processing is achievable for electrode production with Parafilm. It is relatively facile to dry mixing process at 25 °C. Furthermore, it allows feasible cohesion of the active materials to be interconnected by mild pressing and can help save energy during fabrications.

A potential concern with using Parafilm as a binder might be low thermal stability. However, because it is a blend of paraffin and PE

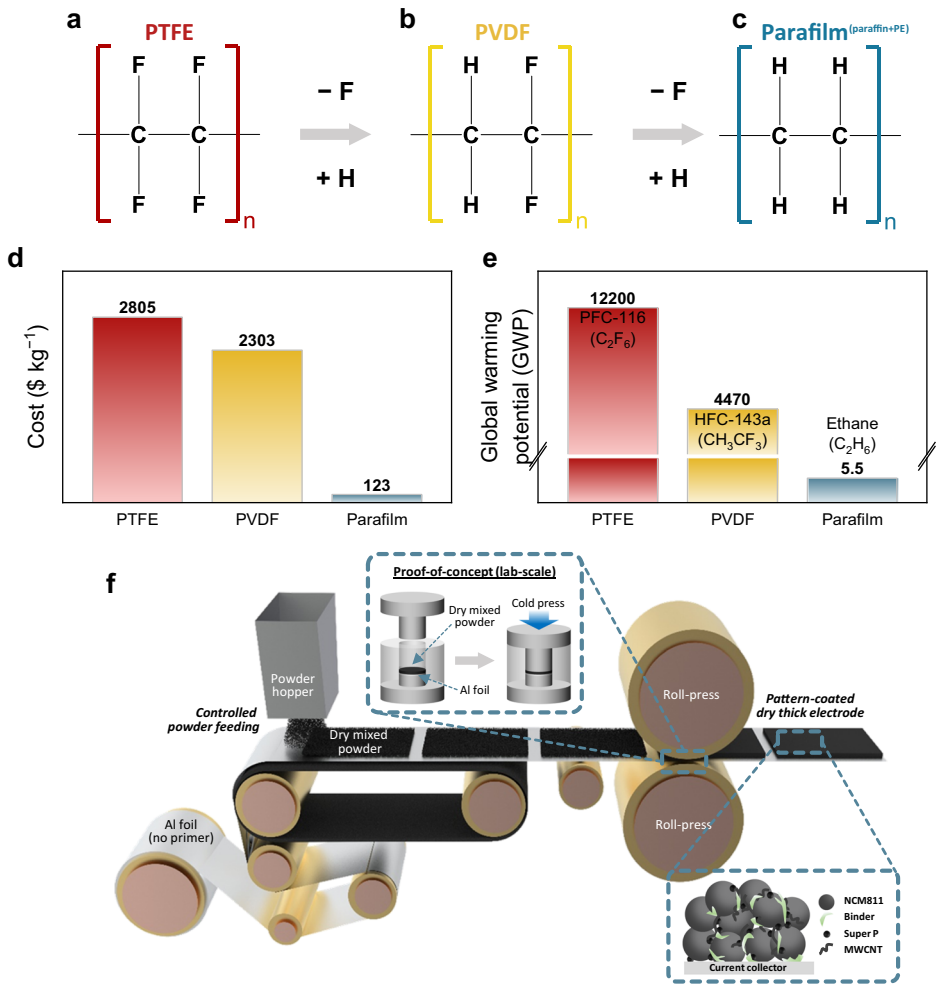

Fig. 1 | Design of binders from an environmental perspective and image of emerging manufacturing process. Comparison of PTFE, PVDF, and Parafilm binders based on structure, cost, environmental impact, and manufacturing process. **a**–**c** The binder chemistry comparison represents the molecular structure. The comparisons of **d** materials cost and **e** GWP to identify the economic and environmental impact. **f** The potential fabrication process schematics on the powder-to-electrode concept involved pressing and pattern-coated electrode formation.

https://doi.org/10.1038/s41467-025-66082-3

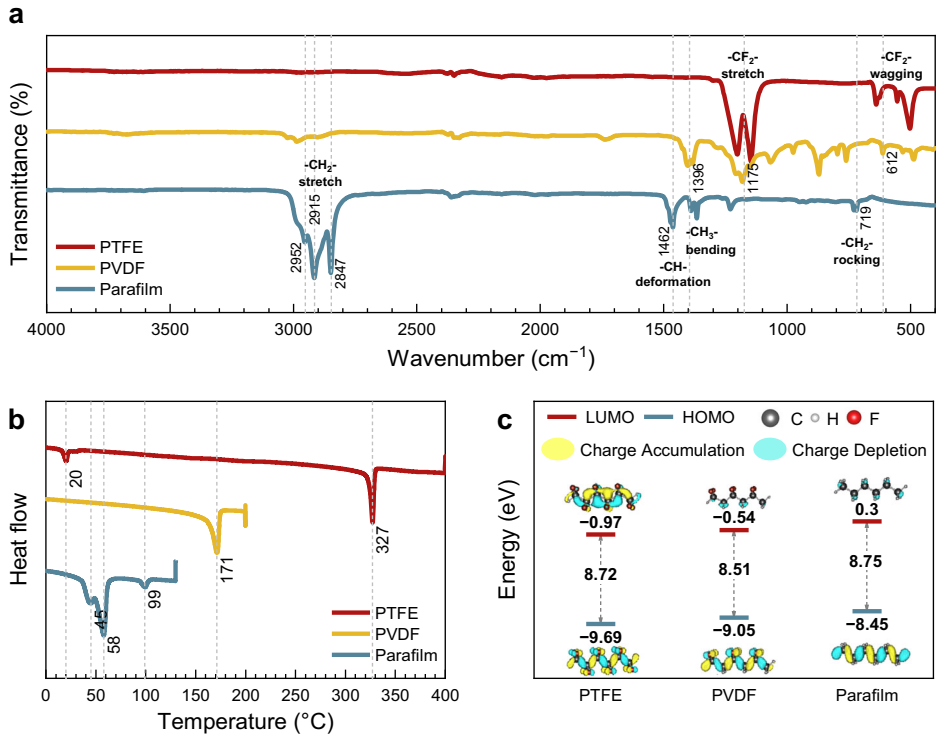

Fig. 2 | Chemical and thermal property analysis of PTFE, PVDF, and Parafilm binders. a FTIR spectra demonstrating C-F and C-H bond signals. **b** DSC curves featuring T_g of binders. **c** HOMO-LUMO energy gap of polymer segments estimate an electrochemical window.

(Fig. 2a), Parafilm is unlikely to the typical paraffin. While pure paraffin is liquified when heated, this synthetic mixture becomes sticky and cheesy under substantial heating, as shown in Supplementary Fig. 2. Consequently, this behavior alleviates concerns regarding binder stability at high temperatures. The subsequent section discusses the comparative testing results of thermal stability on both the electrodes and cells with those binders.

Another factor relevant to the long-term reliability of electrodes is the electrochemical stability of binder materials. Figure 2c shows the density functional theory (DFT) calculation of the energy gap of the repeating units for PTFE, PVDF, and Parafilm by targeting their highest occupied molecular orbital (HOMO) and lowest unoccupied molecular orbital (LUMO). The atomic coordinates of the optimized computational models are provided in Supplementary Data 1–3. As the degree of fluorination decreases, the overall energy levels tend to be upshifted. Accordingly, Parafilm exhibited the widest electrochemical window among the three binders, especially concerning its highest LUMO level, making this material also suitable for negative electrode application. Due to the strong symmetric C-H sigma bonds in Parafilm, it is known to be electrochemically inert and, hence, will not undergo any undesirable side reactions during the battery operation. This stability makes Parafilm-based electrodes relatively compatible for working with both negative and positive electrodes. To confirm the electrochemical stability of those binders to validate the DFT calculation, linear sweep voltammetry (LSV) was tested. The LSV has been scanned at a rate of 1 mV s^{-1} in a potential window from 0 to 5 V vs. Li^+/Li. As seen from Supplementary Fig. 3, Parafilm binder has indicated robust electrochemical stability up to 5 V vs. Li^+/Li, which was better than PTFE, whose oxidative stability was only up to about 4.6 V vs. Li^+/Li, which was different from the DFT calculation due to the unspecified reason. PTFE also showed an electrochemical reduction at 0.7 V vs. Li^+/Li, which is commonly raised concern at the low voltage range. These results indicate that the Parafilm binder is relatively electrochemically stable compared to the other types of binder.

Microstructural integrity of wet and dry thick electrodes

The critical factors that affect electrochemical performance and cycle life in LIBs are the mechanical integrity and microstructural features of binder materials. Figure 3 presents a detailed comparison between PTFE, PVDF, and Parafilm concerning adhesion and cohesion properties and the microstructural distribution in the electrodes. We fabricated electrodes based on their conventional wet or dry method with each binder to assess the impacts of both materials and processes. Given the differences among the true densities of PTFE (2.2 g cm^{-3}), PVDF (1.78 g cm^{-3}), and Parafilm (0.92 g cm^{-3}), the binder content was adjusted to have the same volume ratio rather than by weight ratio (Supplementary Table 2, Supplementary Fig. 4a). Scanning electron microscope (SEM) images (Supplementary Fig. 4b–c) reveal that, at 2 wt%, the Parafilm binder considerably covers the surface and agglomerates, suggesting excessive addition. At 1 wt%, however, it partially coats the active material surface, which can facilitate lithium ion mobility. At 5 wt%, it was found that a Parafilm-based electrode can be freestanding without a current collector, similar to the PTFE-based one as shown in Supplementary Fig. 5. However, such a high content of binder can dilute the benefits of dry electrodes, which is impractical in terms of energy density. Consequently, binder content was carefully adjusted for testing.

Surface and interfacial cutting analysis system (SAICAS) was employed to evaluate the binding characteristics of the electrodes[42–44]. Figure 3a, b presents the results for cohesion and adhesion measured by SAICAS. In Fig. 3a measurements were conducted at depths of 30, 60, and 90 µm to assess internal cohesion between the components within the electrode structure. The PTFE-based electrode exhibited relatively uniform cohesion values of approximately 0.3 N mm^{-1} across all depths. In contrast, the PVDF-based electrode showed a value of ~ 0.2 N mm^{-1} at 30 µm, but cohesion sharply decreased closer to the current collector interface. This trend reflects the significant CBD migration that occurs during solvent evaporation in wet processing, which can also be seen in Fig. 3d, g. The Parafilm-based electrode maintained an average cohesion value over 0.2 N mm^{-1}, comparable to

https://doi.org/10.1038/s41467-025-66082-3

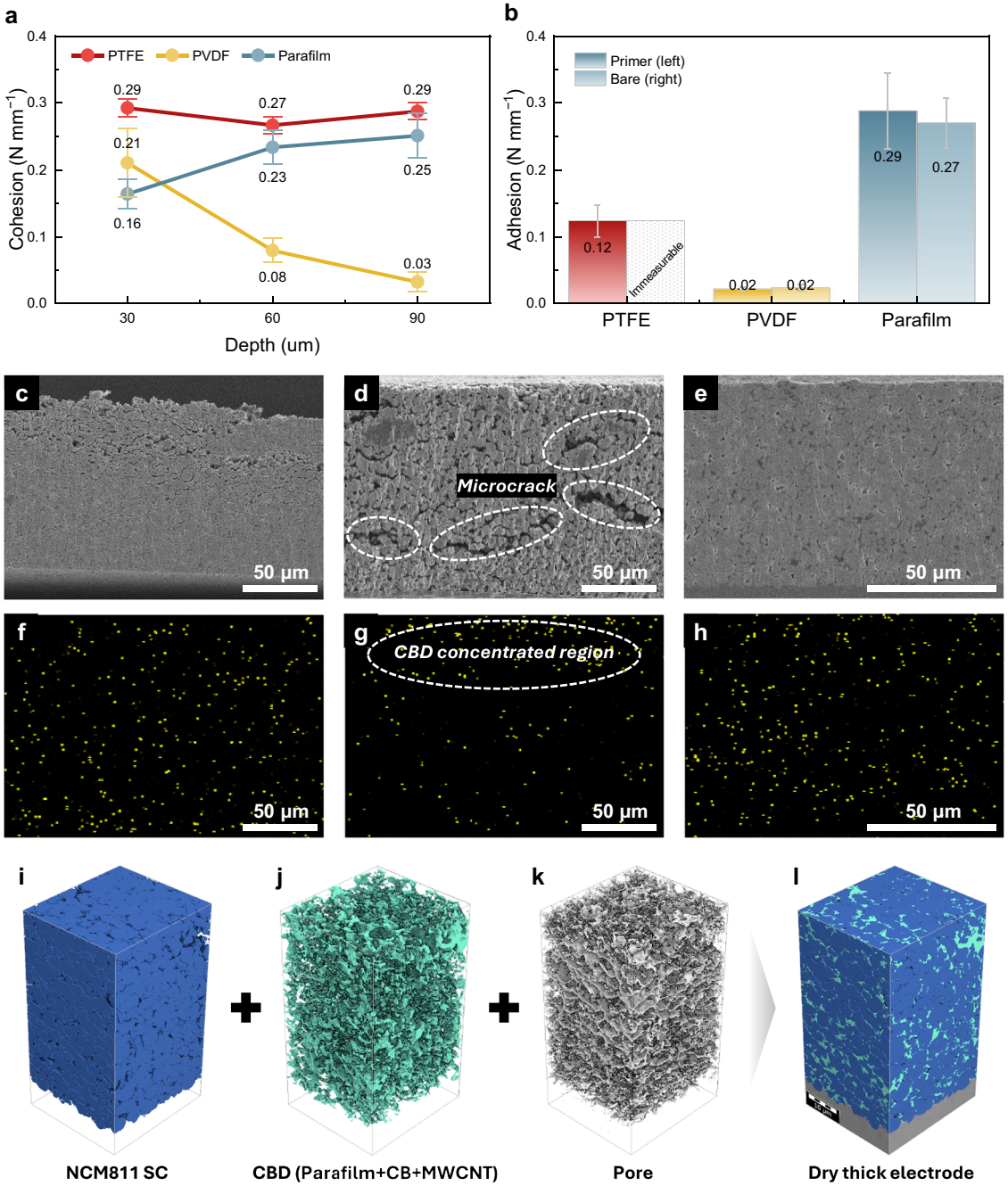

Fig. 3 | PTFE, PVDF, and Parafilm binders comparison by mechanical properties. a Depth-dependent cohesion measurement of electrodes **b** Adhesion measurement with and without primer coating. The error bars represent the standard deviation (σ) from three independent measurements for each experimental group. The adhesion and cohesion values were determined as the averaged horizontal force measured within the defined loading region. The cross-sectional SEM and C atom EDS mapping images of **c**, **f** PTFE, **d**, **g** PVDF, and **e**, **h** Parafilm-based ones were used to determine the CBD distribution and microstructural defects. **i**–**l** 3D reconstructed image from FIB-SEM analysis for the microstructure and material distribution of Parafilm-based dry electrodes.

PTFE within the error range. The lower cohesion observed near the surface (30 μm) can be attributed to the asymmetric density gradient inherent to the powder-to-electrode process, which employs single-action compaction. In this method, the compaction pressure decreases from the top toward the bottom of the compact[45]. This non-uniform stress distribution through the thickness may result in lower cohesion values at the electrode surface. Figure 3b presents the adhesion measured at the interface between the electrode and the current collector, evaluated both with and without a primer coating. For PTFE, electrode fabrication on a bare current collector was not feasible, and thus the corresponding data is marked as immeasurable. The measured adhesion strength of PTFE was lower than its cohesion, suggesting that its fibrillation does not significantly enhance interfacial adhesion. PVDF exhibited poor adhesion regardless of the presence of a primer layer, representing the inherent difficulty of fabricating thick electrodes via wet processing. In contrast, Parafilm demonstrated adhesion values over 0.3 N mm^{-1}, irrespective of primer coating. These results indicate that Parafilm serves effectively in both cohesion and adhesion roles. The raw SAICAS data are provided in Supplementary Fig. 6, with corresponding measurement images shown in Supplementary Fig. 7. Based on Supplementary Fig. 8, adsorption energies increase with polymer chain length, due to a larger contact area. PTFE

had the weakest interaction with the current collector, while PVDF and Parafilm showed stronger adsorption. PVDF is wet-processed, and Parafilm is dry-processed. Despite strong theoretical interactions with aluminum, actual adhesion may be hindered by carbon-binder migration during drying.

As previously discussed, not only interfacial adhesion but also internal cohesion is critical for electrode integrity. As shown in the SEM and energy dispersive spectrometer (EDS) images in Fig. 3c, f, the PTFE-based dry electrodes exhibited good cohesion without noticeable cracks, indicating a homogeneous microstructure. In contrast, for the PVDF-based wet electrodes in Fig. 3d, g, some defects and non-uniform distribution of CBDs could be detected. These defects indicate poor cohesion, likely to cause non-uniform electrochemical activity and further accelerated degradation. However, Fig. 3e, h show that the Parafilm-based dry thick electrode has better structural integration, and the CBD was distributed uniformly within the electrodes. Such even distribution can ensure mechanical robustness, improving uniform electrochemical reactions. As shown in Supplementary Table 3, we additionally performed folding tests with PTFE-, PVDF-, and Parafilm-based electrodes to severely check the adhesion. The PTFE-based electrodes completely delaminated upon folding. For the PVDF-based one, even observable cracks were found on the folded edges, but it was confirmed to have a suitable attachment. Interestingly, high lamination of the Parafilm-based electrode was maintained even after using such severe folding stress. Fewer cracks appeared with no detachment from the Parafilm-based ones. In addition, we also examined the contact angle of the liquid electrolyte on the electrode surfaces. Those results show that the wettability of the Parafilm-based one was better than that of the PTFE- and PVDF-based one[46]. We speculated that this is because of the formulation of Parafilm with PE, even the typical paraffin is known to be hydrophobic. This property could turn out to be critical, especially for electrodes with large areas, high loading, and high density.

Figure 3i–l presents three-dimensional reconstructed images acquired by focused ion beam (FIB)-SEM to evidence the distribution of deconvoluted electrode materials along the thickness direction. The thresholds were determined using *k*-means clustering, with Supplementary Fig. 9. Applying state-of-the-art imaging methodology has exposed Parafilm-based dry electrodes with a uniformly constructed microstructure and distribution. The extracted cross-sectional images every 10 µm confirm that the spatial distribution of active materials, CBD, and pores was highly uniform (Supplementary Fig. 10). The evenly dispersed CBD might prevent micro-defects by reducing the potential for localized stress concentrations that could lead to failure and cause degraded performance over time.

Additionally, we directly scorched the electrodes to examine their thermal stability. After torching the electrodes for one minute, visible damage, such as cracks or detachment and the ignition of binder, was not observed for all binder cases (Supplementary Fig. 11, Supplementary Movie 1–3). The electrode microstructures were almost identical even under flame exposure above the T_g, indicating that the Parafilm binder was phenomenologically similar to the other commercial PTFE and PVDF binders at significantly elevated temperatures as well. Interestingly, scorching the Parafilm electrode caused the formation of unknown liquid droplets around the electrode (Supplementary Movie 3). Based on the thermogravimetric analyzers (TGA) result in Supplementary Fig. 12, we infer that these droplets represent water as a byproduct of Paraffin combustion. This high temperature stability of Parafilm as a dry electrode binder was unexpected, given its low T_g. As is known, Parafilm is a mixture of paraffin and PE, it is likely to have an upshifted thermal stability compared to pure paraffin. The detailed reason why Parafilm exhibits substantial thermal stability and how to further enhance it for higher temperatures to improve safety should be further studied at this stage. This feature highlights an additional environmental advantage, in case of battery thermal runaway, conventional binders such as PTFE and PVDF release toxic fluorinated gases[47,48], but Parafilm, which is fluorine-free, would primarily decompose into relatively non-toxic byproducts like hydrocarbons and water.

Ionic transport kinetics in the wet and dry thick electrodes

Charge transfer and ionic transport are important behaviors in understanding the kinetics in the electrodes[49]. To investigate ionic transport, we evaluated and compared the ionic tortuosity of the electrodes. For this purpose, an electron blocking symmetric cell was assembled, consisting of two identical electrodes fabricated with the same binder. The primary role of the electron-blocking configuration is to suppress electronic conduction at the electrode–electrolyte interfaces. This prevents electrons from participating in interfacial electrochemical reactions, thereby focusing on ionic transport behavior within the electrolyte phase. Impedance spectroscopy was performed using this symmetric cell, and the ionic resistance (R_{ion}) was extracted by fitting the data to the equivalent circuit shown in Supplementary Fig. 13. The tortuosity was then calculated by applying R_{ion} to Eq. (1). As shown in Fig. 4a, the electrochemical impedance spectroscopy (EIS) data for PTFE-based electrodes exhibit a small semicircle, indicating low charge transfer resistance. This means that PTFE provides an efficient pathway for charge transfer due to the fibrilized microstructure of the binder (Supplementary Fig. 14a). It opens the interface between the active materials and the electrolyte, facilitating charge transfer without physical barriers. In contrast, the charge transfer resistance for PVDF-based electrodes was significant, as observed by the larger semicircle shown in Fig. 4b. This might be possible due to the film-like morphology of the PVDF binder on the active materials (Supplementary Fig. 14b), which hinders charge transfer at the interface between the active materials and the electrolyte. Figure 4c shows that Parafilm-based electrodes also exhibit a small semicircle similar to that measured for PTFE, suggesting low charge transfer resistance. The errors ($\boldsymbol{\chi^2/|Z|^2}$) between the raw and fitted data for Fig. 4a–c, as well as the tortuosity values describing ionic transport pathways in the porous electrodes, are reported in Supplementary Table 4. Figure 4d shows that PVDF-based electrodes have the highest tortuosity, indicating complex and inefficient ionic transport. This can also be explained by the blocked interface by the covered binder film as shown in Supplementary Fig. 14b. In contrast, Parafilm-based electrodes exhibit the lowest tortuosity and have an effective ionic transport pathway. Interestingly, Parafilm was found not to swell in the liquid electrolyte after long-term immersion, as shown in Supplementary Fig. 15. The contrasting tortuosity values observed between the two binders can be attributed to the CBD inhomogeneity of the PVDF-based electrodes compared to that of Parafilm. Both PVDF and Parafilm exhibit a film-like morphology on the surface of active materials, and PVDF can be swelled in the presence of the liquid electrolyte. However, the higher concentration of CBD near the electrode surface with a slurry-casted PVDF-based electrode can hinder ion transport within the electrodes, potentially inducing increased ionic tortuosity. The reduced tortuosity in Parafilm-based electrodes can provide direct routes for ions to move through, potentially improving electrochemical kinetics[50].

Direct current internal resistance (DCIR) is another critical parameter defining the comprehensive resistance of the electrodes including charge transfer and ionic transport. Figure 4e shows a trend of Parafilm-based electrodes having the lowest internal resistance (IR), followed by PTFE and PVDF at 50% of the state of charge (SOC). This complies with the former impedance and tortuosity findings in that Parafilm has the most efficient charge transfer and ionic transport for conductive pathways. The relaxed potential after DCIR measurement also provides other kinetical information, as shown in Fig. 4f–h. After turning off an applied pulse current, the voltages of the electrodes were relaxed to their quasi-equilibrium state. The rate of this relaxation

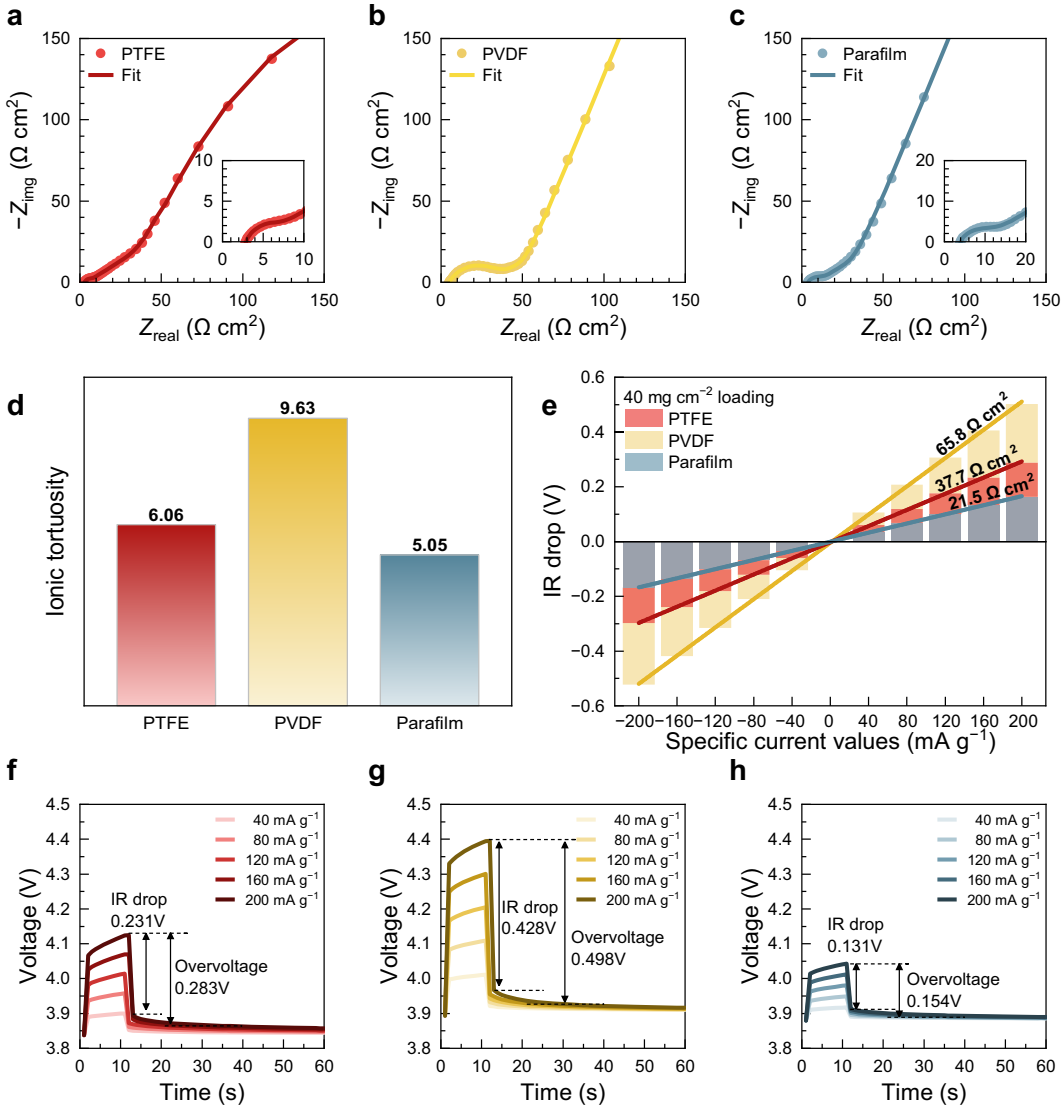

Fig. 4 | Charge-transfer and ionic transport kinetics of PTFE, PVDF, and Parafilm binder-based electrodes at 25 °C. Nyquist EIS data for **a** PTFE, **b** PVDF, and **c** Parafilm-based electrodes. **d** The ionic tortuosities and **e**–**h** DCIR comparison for those binder-based electrodes to identify the comprehensive resistance. (1 C = 200 mA g^{-1}).

reflects the kinetics of charge transfer and ionic transport through the electrolyte and porous electrode structures or the ionic diffusion. Thus, the PTFE and Parafilm-based electrodes show rapid relaxations to the equilibrium, implying facile ionic transport and charge transfer compared to that of PVDF. We further measured ionic diffusivity based on galvanostatic intermittent titration technique (GITT), presented in Supplementary Fig. 16. The curves regarding charge/discharge overvoltage were almost similar to those of PTFE, PVDF, and Parafilm, so the lithium-ion diffusivities were also nearly identical. The ionic diffusivities of the Parafilm binder showed a slightly lower diffusivity than others. This is likely due to the Parafilm partially coating the active material surface during the mixing, which can hinder lithium ion transport compared to other binders (Supplementary Fig. 14d). This phenomenon indicates that the ionic transport through the partially blocked porous structure of the Parafilm-based electrode was slightly impeded than the PTFE-based one but showed similar charge transfer if the ions reached the electrode|electrolyte interface.

Meanwhile, to assess the electronic conductivity of the electrodes, we measured resistivity with results in Supplementary Table 5. PTFE had slightly better conductivity than Parafilm, but the difference was minor. In-plane conductivity was evaluated through interface resistance, showing that Parafilm had lower resistance, indicating better adhesion to the current collector than PTFE. The interfacial resistance for the PVDF-based electrode was not measured due to delamination. Overall, Parafilm offers stable electrode formation without primer and is a viable fluorine-free alternative to PTFE for thick dry-processed electrodes.

Electrochemical performance of wet and dry electrodes

The electrochemical performance of LIB electrodes, especially in terms of rate capability and cycling stability, could directly reflect the practical application of LIB binders. Figure 5 provides a detailed comparison of the behavior of PTFE, PVDF, and Parafilm binders under various current rates and long-term cyclic conditions. Figure 5a illustrates the rate capability of PTFE-based electrodes in a half-cell configuration (Supplementary Fig. 17). PTFE shows a relatively flat capacity retention at different specific current. Generally, the stable performance of PTFE under these conditions can also be attributed to a sufficiently broad pathway for charge transfer and ionic transport, as hinted previously by the results from EIS in Fig. 4. This consistent rate performance makes PTFE a reliable binder despite its drawbacks related to poor adhesion and mechanical issues under electrochemical operation. Figure 5b presents the rate capability for the PVDF-based electrodes, but it showed some degraded rate performance compared

https://doi.org/10.1038/s41467-025-66082-3

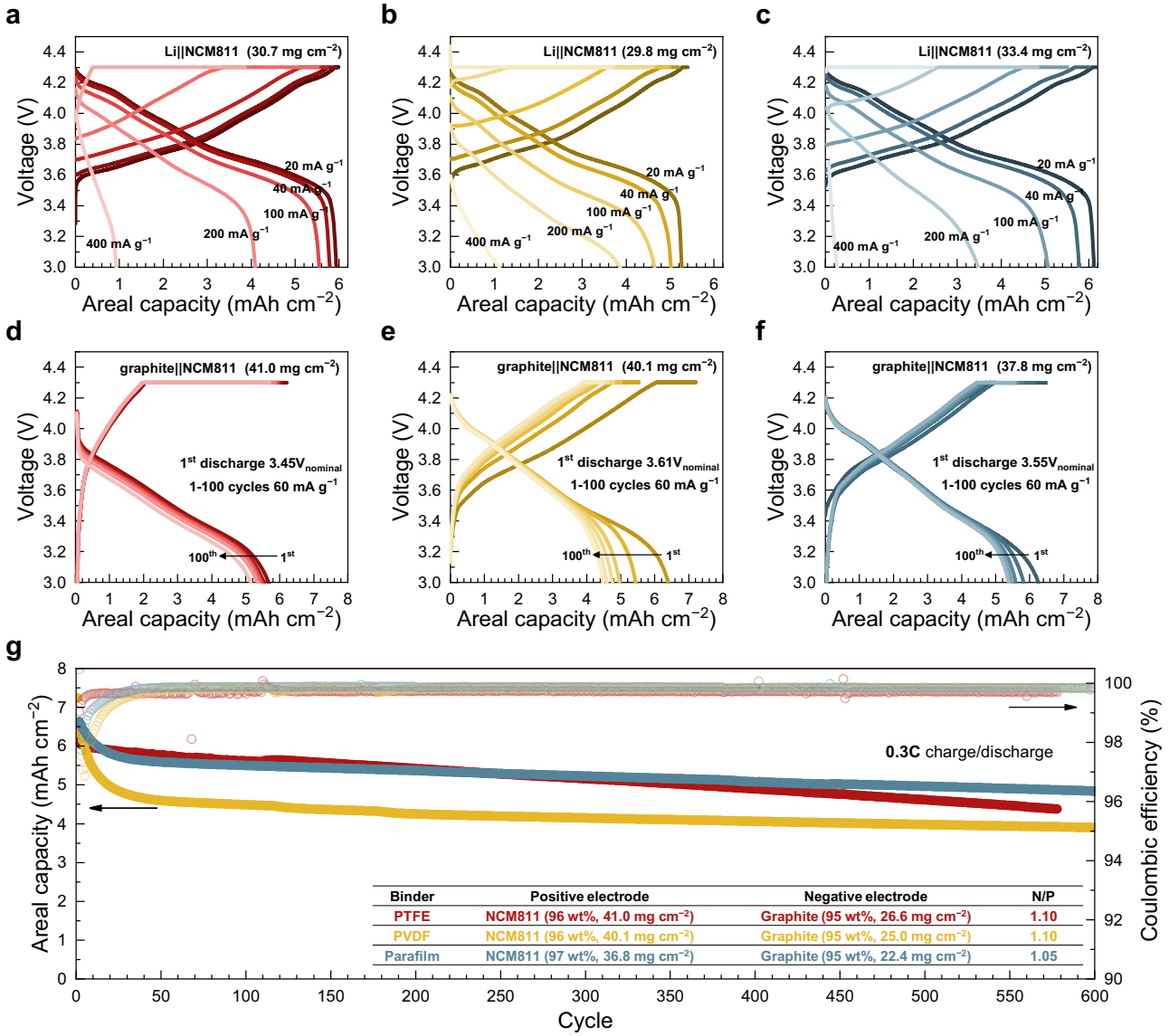

Fig. 5 | Electrochemical evaluation for PTFE, PVDF, and Parafilm binder-based electrodes at 25 °C. Rate capabilities in half-cell configuration for **a** PTFE, **b** PVDF, and **c** Parafilm. The cycling profile of full cells with **d** PTFE, **e** PVDF, **f** Parafilm, and **g** the cyclability comparison, where the PTFE cell failed after 580 cycles. (1 C = 200 mA g^{-1}).

to PTFE, especially at the high rate, reflecting increased overvoltage from 200 mA g^{-1}. The relatively large semi-circle seen in the EIS plot in Fig. 4b might point to higher charge transfer resistance that becomes more pronounced as the specific current increases. It reflects the structural limitations of PVDF, particularly about film-like types of morphologies that PVDF tends to form, causing blockage of efficient ion flow at higher currents. Meanwhile, Parafilm shows acceptable capacity at lower specific current but decays after 200 mA g^{-1}.

This is unexpected, given the low tortuosity of Parafilm-based electrode noted in Fig. 4. However, different operating conditions between the tests can also explain this apparent inconsistency. EIS and tortuosity analyses typically measure corresponding properties at low alternative currents correlated with the galvanostatic results at low rates. Those analyses may deviate, however, from the charge transfer and ion transport kinetics at high galvanostatic specific current. The DCIR result in Fig. 4e–h aligns the initial IR drop of the rate testing results at 200 mA g^{-1}, which started to discharge at about 3.9 V (PVDF) and 4.0 V (Parafilm). Nevertheless, it still showed that the overall overvoltage of the Parafilm-based electrode was slightly inferior to that of the PVDF-based. As Supplementary Fig. 14 visualizes the surface morphologies of electrodes with different binders, the slightly sluggish overall ionic diffusion kinetics evidenced in Supplementary Fig. 16 can explain this result. Addressing this issue may require further investigation of dry electrode mixing protocols.

In this context, we additionally conducted a continuous twin-screw-based dry mixing with a Parafilm-based binder, as shown in Supplementary Fig. 18. The dry mixing was repeated three times to obtain the homogenized dry mixed composite powder with Parafilm (Supplementary Fig. 18b–d). The first discharged powder in Supplementary Fig. 18b and Supplementary Movie 4 was relatively fine, indicating the powder cohesion was insufficient, as confirmed in the inset of the compound clumping and the mechanically weak electrode. However, the second and third iterations of the dry mixing in Supplementary Fig. 18c–d and Supplementary Movie 5–6 showed dramatically increased powder cohesion and granulation, facilitating compounding and electrode fabrication. Although the continuous dry mixing was successful by visual inspection, its microstructure was not optimal regarding the CBD distribution and the mechanical fracture of the NCM811 single crystal, as shown in Supplementary Fig. 18e–f. Because of these results, the initial electrochemical properties might slightly deteriorate regarding the discharge capacity outcome in Supplementary Fig. 18g. Therefore, the dry mixing can also

significantly impact the quality of the electrode and the electrochemical performance, so further optimization will be required.

Figure 5d–g presents the full-cell configuration cycling profile of the electrodes at 0.3 C. In Fig. 5d, the PTFE-based electrodes exhibit stable cycling performance, with a gradual capacity decline observed up to 100 cycles. In contrast, the PVDF-based electrodes show a noticeable capacity fade starting within the first 10 cycles. This can be ascribed to sluggish charge transfer and ionic transport kinetics that would induce non-uniform electrochemical reactions within the thick electrode. However, Parafilm-based electrodes have decent cycling stability up to 1000 cycles (Supplementary Fig. 19) and the coulombic efficiency was converged to over 99.8 %, meaning that Parafilm may well-operate under a galvanostatic condition with resisting mechanical and electrochemical stresses during the cycling as shown in Fig. 5f. Furthermore, the specific energy and energy density of the positive electrodes were calculated, although those were mode of coin-cell format. Both the specific energy and energy density were higher for the electrode using the Parafilm binder. This is because not only does the low density of the Parafilm itself enhance the high specific energy, but also the fabrication of a dense electrode with Parafilm contributes to the high energy density as shown in Supplementary Fig. 20 as calculated from the first-cycle capacity values in Fig. 5g, noting that higher porosity reduces energy density as shown in Supplementary Table 6. PTFE and Parafilm electrodes had about 15% porosity, while the PVDF electrode had 30%. This difference stems from the fabrication processes, and efforts to reduce PVDF porosity caused delamination, complicating comparisons. The strong cyclability and energy density exhibited by Parafilm could be due to a distinctive combination of binder chemistries and mechanics that provide structural solid integrity and electrochemical/chemical stability. This makes Parafilm an attractive alternative dry electrode binder in producing high-efficiency batteries through sustainable manufacturing. The detailed information is provided in Supplementary Table 7–8.

As shown in Supplementary Fig. 21, the PTFE-based electrode exhibited a short constant current (CC) charging phase, with most of the charge capacity obtained during the prolonged constant voltage (CV) phase. By the 100th cycle, the CV charge ratio accounted for approximately 70% of the total capacity. This increasing reliance on CV charging is indicative of accelerated performance degradation accelerates[51]. Some previous literatures indicate that in CC-CV charging, 94.5% of lithium inventory is lost in the CV stage[52]. In contrast, PVDF and Parafilm cells show a CV charging ratio of 15% to 20%. The PVDF cell displays a normal CC/CV profile but a rapid decrease in discharge capacity, which is typical of high-loading wet electrodes (Fig. 5e). However, the Parafilm cell relatively maintained its capacity (Fig. 5f), which was highly effective cycle stability up to 1000 cycles. As shown in Supplementary Fig. 22, when the PTFE cell was electrochemically tested as a half cell, the charge/discharge profile was normal even at a loading of 60 mg cm^{-2}. In a half cell, there are no restrictions on the lithium source since lithium metal is used as the counter electrode, allowing isolated observation of the positive electrode behavior. In a full cell, however, the behaviors of the positive electrode and negative electrode are interdependent. Additionally, since full cells rely solely on lithium ions in the positive electrode, irreversibility significantly affects performance. Thus, operating the thick electrode at 0.3 C can be impacted by both positive electrode and negative electrode overvoltages. While negative electrode overvoltage and its effects are not the main scope of this work, these issues should be addressed through further research.

To identify the initial impact of binders on cathode electrolyte interphase (CEI) layers, C 1*s*, F 1*s*, and O 1*s* XPS spectra were collected after 1st discharge in Supplementary Fig. 23. In the C 1*s* spectra, the representative CF_2 peak for the fluorinated binders showed that PTFE had a strong peak, while PVDF had a relatively low one. Those binders exhibited similar peak intensities for the C-C bond, as well as other peaks such as C=O and Li_2CO_3, which are typically observable in CEI layers. In contrast, Parafilm exhibited only a strong C-C bonding signal (284.5 eV) without any fluorine-related features, reflecting the fluorine-free nature of the saturated hydrocarbon backbone. This finding is well-aligned with the chemistries of those binders, indicating that the chemical nature of the CEI layer is highly dependent on a specific binder. In the spectra of F 1*s* and O 1*s*, it was possible to observe LiF, Li_2CO_3, and many more. These are commonly found in CEI layers formed by conventional liquid electrolytes with fluorinated lithium salts and additives. We should still note that PTFE showed a prominent -CF_2CF_2 peak, while Parafilm had no trace at that position, which indicates that the CEI layer is highly correlated with the binder chemistries, as seen in the C 1*s* spectra. The moderate CV charge capacity ratio suggests indirect evidence of CEI layer formation of Parafilm[53,54]. These results imply that Parafilm not only maintains structural integrity but also supports the formation of a comparable CEI layer.

To further validate the applicability of the Parafilm binder in practical systems, we conducted a pouch cell-based demonstration (Supplementary Fig. 24). An electrode with a size of 3 cm × 4 cm, using Parafilm as the binder, was prepared, and a pouch cell was assembled using 20 µm-thick lithium metal as the counter electrode. The cell was cycled at 20 mA g^{-1}, and a noticeable decline in capacity was observed after approximately 30 cycles. We found that this capacity degradation arises from the uneven plating and stripping of lithium metal, which eventually causes the depletion of the inventory, leading to the exposure of Cu current collectors. To determine whether the capacity degradation was caused by the Parafilm-based electrode, the cycled pouch cell was disassembled, and then the positive electrode was recovered and reused in a coin cell for further testing. The coin cell with the reused positive electrode showed recovered capacity and remained stable for an additional 50 cycles. These results confirm the practical viability of Parafilm as a binder for dry thick electrodes, even when scaled up to large areas (Supplementary Fig. 25).

Notably, we also evaluated the electrochemical stability of the electrodes at 70 °C, which exceeded the T_g of Parafilm as shown in Fig. 2b. As shown in Supplementary Fig. 26, the electrode with Parafilm maintained more stable initial capacities, even after torching compared to the electrodes using other binders. Combined with the presented results from material, electrode, and cell level perspectives to assess the high temperature behavior of Parafilm as a dry electrode binder, the concern about low T_g can be excluded. Additionally, single-crystalline NCM622 was also tested (Supplementary Fig. 27), achieving an initial capacity of over 7 mAh cm^{-2}. The electrode density of NCM622 was lower, at approximately 3.2 g cm^{-3}, compared to NCM811 (3.7 g cm^{-3}), likely due to its smaller particles. Thus, it was found that Parafilm effectively acts as a universal dry electrode binder for the various positive electrode chemistries.

This work has demonstrated the potential of Parafilm as a fluorine-free binder for dry electrode manufacturing in LIBs. Compared to binders like PTFE and PVDF, it has huge advantages over environmental, chemical, mechanical, and electrochemical benefits. Through detailed analysis, Parafilm was validated as an alternative that addresses most of the limitations related to conventional binders. The apparent structural simplicity of Parafilm, with no fluorine, not only reduces its environmental footprint but also enhances its chemical and electrochemical stability. The lower T_g would allow low-energy processing without a primer layer with robust microstructure. The electrochemical kinetics of charge transfer and ionic transport showed efficiency for the Parafilm-based electrodes, but it has some limitations in high C-rate conditions. However, the Parafilm-based dry thick electrode outperformed in cycling stability compared to the other binders, which fully substantiated over 1000 cycle. While additional efforts are still required to optimize the chemistries, Parafilm-based binders could provide momentum to drive the sustainability of battery manufacturing to reach a place in the greener energy storage landscape.

Methods

Materials

The positive electrodes were composed of 97 wt% $LiNi_{0.8}Co_{0.1}Mn_{0.1}O_2$ single crystal (NCM811, SMLAB) as active material, 1.5 wt% carbon black (CB, EQ-Lib-Super P, Timcal), 0.5 wt% multi-walled carbon nanotube (MWCNT, MR99, Carbon Nano-Material Technology Co., Ltd), and 1 wt % binder. Three types of binder were used including Parafilm (Parafilm® M All-Purpose Laboratory Film, Amcor), PTFE (F-104 and F-208, Daikin), polyvinylidene fluoride (PVDF) (KF9700, Kureha). Parafilm was frozen with liquid nitrogen and pulverized to make a powdery form (Supplementary Fig. 28, Supplementary Table 9). Among these, electrodes were manufactured with 1 wt% of Parafilm and 2 wt% of PTFE and PVDF. The negative electrodes were composed of 95 wt% graphite (PAS-CP1, POSCO Future M) as active material, 2 wt% carbon black (EQ-Lib-Super P, Timcal), 1.5 wt% styrene butadiene rubber (SBR, BM451B, Zeon) binder solution (contains 40 wt% SBR and 60 wt% of water), and 1.5 wt% carboxymethyl cellulose (CMC, CMC2200, Daicel Finechem Ltd.) binder solution (contains 1.3 wt% CMC and 98.7 wt% of water).

Electrode preparation

The dry powder with Parafilm as a binder was mixed at 25 °C without solvent with Thinky mixer (ARE-310, Thinky) for a lab-scale (15 g). First, the active material and conductive agents were premixed at 1500 rpm for 2 min and 2000 rpm for 5 min. Then, the binder was added and mixed three times at 1500 rpm for 5 min. For larger batch preparations (100 g), a powder mixer (PLS-300, KMTech) was used. The active material and conductive agent were added first and premixed at 14,000 rpm for 3 min, followed by a 30 s rest, repeating this cycle three times. Subsequently, the binder was added, and the mixing process was repeated six times under the same conditions. The dry mixed powder was placed into a mold and leveled, after which a 20 µm thick primer-free aluminum foil was placed on top. The leveled powder was then pressed at 25 °C using a uniaxial press (QM900L, QMESYS) at 270 bar for 15 s to produce dry positive electrodes.

The dry positive electrode production using PTFE was executed with 100 g batches. Before mixing, the conductive agents consisting of MWCNT and CB were premixed utilizing a powder mixer at 5000 rpm for 9 min. The lab-scale equipments used in the dry electrode manufacturing process included powder mixer (LS-300, KMTech), kneader (NEP-0.5 K, KMTech), roll mill (KRM-80D, 84 KMTech), and roll press (MP-230H, Rohtec) laminating the electrode film onto a carbon-coated aluminum foil (15 µm thickness) with CB-based primer coating layer (1 µm thickness)[55].

The wet positive electrodes were made with active material, conductive agents, and PVDF binder. The binder solution was prepared PVDF dissolved in *N*-methyl-2-pyrrolidinone (NMP, Sigma-Aldrich) as a solvent. The binder solution and conductive agents were first added to Thinky mixer container, followed by a small amount of NMP to adjust the viscosity. The binder solution and conductive agents were first mixed using Thinky mixer at 2000 rpm for 5 min. Subsequently, the active material was added, and the slurry was mixed again under the same conditions to obtain the final slurry. The slurry was coated on the aluminum foil and dried at 80 °C for 12 h under vacuum.

The negative electrode electrodes were fabricated using a wet process with Thinky mixer (ARE-310, Thinky). First, the conductive agents and active material were premixed in a mortar. Next, the CMC binder solution was added and mixed at 1500 rpm for 2 min, followed by 2000 rpm for 5 min. Subsequently, the SBR binder solution was introduced, along with 0.1 wt% of deionized (DI) water based on the total batch size to adjust the viscosity after which it was mixed at 2000 rpm for 2 minutes and 2200 rpm for 1 min. Finally, the slurry was coated onto a Cu foil and dried at 90 °C for 8 h.

Cell assembly

Coin cells (CR2032 type, SUS 316 L) with a height of 20 mm and a diameter of 32 mm were used. Electrochemical tests were performed using different areal electrode loadings of single-side coating. For cell assembly, the positive and negative electrodes were punched with diameters of 14 mm and 16 mm, respectively. The negative electrodes were either 200 µm thick lithium metal (44 mAh cm^{-2}) or graphite. Single-layer separators with a thickness of 20 µm, porosity of 39%, and an average pore size of 0.027 µm, with a diameter of 19 mm, were used (2320, Celgard). The sizes of the negative electrodes, positive electrodes, and separators were controlled to facilitate lithium insertion and extraction. All cells were assembled in an argon-filled glovebox. The 80 µl of liquid electrolyte with several additives contained 1.3 M lithium hexafluorophosphate ($LiPF_6$) dissolved in ethylene carbonate (EC) / ethyl methyl carbonate (EMC) / diethyl carbonate (DEC) (3:5:2, v/v/v), and + 10% fluoroethylene carbonate (FEC, for stable SEI layers) + 0.5% vinylene carbonate (VC, to improve cycle life) + 1% 1,3-propane-sultone (PS, for overcharge protection) + 0.2% lithium tetrafluoroborate ($LiBF_4$, for increased high voltage stability) was added in all coin cells. The configuration of coin cell architecture is shown in Supplementary Fig. 29.

The Parafilm binder-based pouch cell was fabricated in a dry room with a dew point of −60 °C. The pouch cell employed an areal electrode loading of 33.2 mg cm^{-2} with a single-side active area of 3 cm × 4 cm. Lithium foil (20 µm thickness) was used as the negative electrode. The sizes of the negative electrode, positive electrode, and separator were different. Negative electrode was larger than the positive electrode because the negative electrode should take lithium ions from the positive electrode during the charging, while the separator was made larger than the electrodes to prevent short-circuiting. The electrodes were cut using electrode punching machines with the designed sizes for the negative and positive electrodes, and the separator was cut with a cutter. Afterward, the electrode tabs and lead tab terminals were welded. The aluminum pouch film was molded into the electrode shape, and the depth was adjusted with stoppers according to the total electrode thickness. For sealing, the tab and side of the aluminum pouch film were sealed with dedicated machines. Electrolyte was then injected at an electrolyte-to-capacity (E/C) ratio of 1.5, followed by vacuum sealing to complete the pouch cell assembly.

Characterizations

The molecular weight distribution of the Parafilm was measured using high-temperature gel permeation chromatography (HT-GPC, EcoSEC HLC-8321GPC, Tosoh) equipped with a refractive index (RI) detector. The mobile phase was 1,2,4-trichlorobenzene (TCB) containing 0.04 wt % butylated hydroxytoluene (BHT), and calibration was performed using polystyrene standards. A differential scanning calorimeter (DSC Q200, TA Instruments) was used to find out T_g of the binder at a constant heating rate (5 °C min^{-1}) from −20 °C to 400 °C. To determine the electrolyte wettability of the electrodes, the contact angle meter (Phoenix-300, SEO Co. Ltd.) equipment was used. The chemical functional groups were identified using FT-IR (Imvenio S, Bruker) spectrometer in the 400 to 4000 cm^{-1} range with ATR mode. The adhesion and cohesion characteristics of each binder were measured by using a universal testing machine (UTM 226, Myungji Tech) and SAICAS (EN-EX, Daipla Wintes). To determine cohesion, a double-sided tape (3 M) was attached to the 20 mm × 50 mm sized electrode, then pulled at 100 mm min^{-1} speed with a 180° angle. To determine adhesion, SAICAS was employed with a boron nitride (BN) blade (width = 1 mm, blade angle = 60°, rake angle = 20°, and clearance angle = 10°) at CL mode (vertical speed = 10 µm s^{-1}, horizontal speed = 1 µm s^{-1}). The morphology and homogeneity of the prepared electrode samples were checked in a field-emission scanning electron microscope/energy-dispersive X-ray spectroscopy (FE-SEM/EDS, JSM-7610, JEOL). The cross-sectional images of the electrodes were acquired by

cryo-FIB (Crossbeam 550, Zeiss) with voxel size of about 30 µm width × 20 µm depth × 60 µm height. The obtained microstructural images were 3D reconstructed by GeoDict 2023 software (Math2Market, Germany).

Computational details

The structures of the PTFE, PVDF, and paraffin models all consist of three monomer units, each containing six carbon atoms. First-principles DFT calculations were performed using the Vienna Ab-initio Simulation Package (VASP)[56–58] for the optimization of polymer structures. The plane-wave cutoff energy was set to 500 eV, and van der Waals interactions were corrected using the DFT-D2 method by Grimme[59]. A Gamma point mesh of 1 × 1 × 1 was used for Brillouin zone integration. The energy convergence criterion was set to 10^{-4} eV, and calculations proceeded until the atomic forces were reduced to below 0.05 eV $Å^{-1}$. The calculation of the polymer's electronic energy levels, including HOMO and LUMO, was performed using the General Atomic and Molecular Electronic Structure System (GAMESS)[60]. Self-Consistent Field calculations were performed using the Restricted Hartree-Fock type, DFT calculations employed the B3LYP functional[61,62], and the basis set used was 6–311 G**+.

Electrochemical tests

The galvanostatic charge/discharge tests of coin half-cells were assessed using a potentiostat (WBCS3000, WonATech) at 25 °C between 3.0 and 4.3 V at 20 mA g^{-1} (1 C = 200 mA g^{-1}). The symmetric cell analysis was made to obtain the intrinsic Li^+ diffusivity and tortuosity of the electrodes. EIS analysis of the symmetric cell was carried out in the potentiostatic mode over the frequency range of 100 mHz to 7 MHz with 6 data points per decade and a sinusoidal amplitude of 10 mV. The tortuosity of the electrodes was obtained from the EIS data by the symmetric cells by Eq. 1. Rates from 20, 40, 100, 200, and 400 mA g^{-1} were tested for 3 cycles, each in the same cut-off voltage range. GITT measurement was conducted with charge/discharge of 20 mA g^{-1} for 30 minutes, followed by an open circuit for 2 hours. The Li^+ diffusion coefficient was calculated by Eq. 2. DCIR was measured at 50% SOC. The pulsed current was applied for each 10 s with rates of ±40, ±80, ±120, ±160, and ±200 mA g^{-1}, rested for 10 min between the charge/discharge. In the full-cell test, the corresponding specific energy and energy density were calculated based on the discharge profile of the first cycle. For each, the calculations were conducted using Eq. 3 and Eq. 4 below. The pouch cell was tested under a compression of 3.74 MPa

$$\tau = \frac{R_{\text{ion}} \cdot A \cdot \varepsilon \cdot \kappa}{L} \tag{1}$$

Here, τ is tortuosity, R_{ion} is ionic resistance, A is area of the electrode, ε is porosity, κ denotes effective ionic conductivity in the electrode, L is the total thickness of the electrodes for ion movement.

$$D = \frac{4}{\pi\tau}\left(\frac{m_B V_M}{M_B S}\right)^2\left(\frac{\Delta E_s}{\Delta E_t}\right)^2 \tag{2}$$

Here, D is diffusion coefficient, τ is the pulse duration, m_B is the mass of the host material in the electrode [g], M_B is the molecular weight of the host material [g mol^{-1}], V_M is the molar volume of the material [cm^3 mol^{-1}], S is the contact area of the electrolyte and electrode interface [cm^2], ΔE_s is steady-state voltage change, ΔE_t is total voltage change during the current pulse.

$$U_W = \frac{Q_{\text{dchg}} \times V_{\text{dchg}} \times A_{\text{positive}}}{w_{\text{positive}}} \tag{3}$$

Here, U_w is the specific energy [Wh kg^{-1}], Q_{dchg} is the areal discharge capacity [Ah cm^{-2}], V_{dchg} is the discharge nominal voltage [V], A_{positive} is the area of positive electrode [cm^2], w_{positive} is the weight of positive electrode [kg].

$$U_v = \frac{Q_{\text{dchg}} \times V_{\text{dchg}}}{T_{\text{positive}}} \tag{4}$$

Here, U_v is the energy density [Wh L^{-1}], Q_{dchg} is the areal discharge capacity [Ah cm^{-2}], V_{dchg} is the discharge nominal voltage [V], T_{positive} is the thickness of positive electrode [cm].

Data availability

The authors declare that all data supporting the findings of this study are available within the paper, its Supplementary Information and Source Data file. Source data are provided with this paper.

References

1. Ritchie, H., Rosado, P. & Roser, M. *Energy Production and Consumption*, https://ourworldindata.org/energy-production-consumption (2020)
2. Degen, F., Winter, M., Bendig, D. & Tübke, J. Energy consumption of current and future production of lithium-ion and post lithium-ion battery cells. *Nat. Energy* **8**, 1284–1295 (2023).
3. Ahmed, S., Nelson, P. A., Gallagher, K. G. & Dees, D. W. Energy impact of cathode drying and solvent recovery during lithium-ion battery manufacturing. *J. Power Sources* **322**, 169–178 (2016).
4. Wood, D. L. et al. Technical and economic analysis of solvent-based lithium-ion electrode drying with water and NMP. *Dry. Technol.* **36**, 234–244 (2018).
5. Entwistle, J., Ge, R., Pardikar, K., Smith, R. & Cumming, D. Carbon binder domain networks and electrical conductivity in lithium-ion battery electrodes: A critical review. *Renew. Sustain. Energy Rev.* **166**, 112624 (2022).
6. Yao, W. et al. A 5 V-class cobalt-free battery cathode with high loading enabled by dry coating. *Energy Environ. Sci.* **16**, 1620–1630 (2023).
7. Zhong, L., Xi, X., Mitchell, P. & Zou, B. Dry particle based capacitor and methods of making same. US patent 7352558B2, filed April 2, 2004, and issued April 1, 2008.
8. Wang, Y., Zheng, Z., Ludwig, B. & Pan, H. Dry powder based electrode additive manufacturing. US patent US20170062798A1 filed August 31, 2016, and issued March 2, 2017.
9. Tschöcke, S. et al. Process for producing a dry film and dry film and dry film coated substrate DE patent DE102017208220A1, filed May 6, 2017, and issued November 22, 2018.
10. Tesla Inc., *Tesla Completes Acquisition of Maxwell Technologies*, https://ir.tesla.com/press-release/tesla-completes-acquisition-maxwell-technologies (2019)
11. Tesla Inc., *2020 Battery Day Presentation Deck*, https://digitalassets.tesla.com/tesla-contents/image/upload/IR/2020-battery-day-presentation-deck (2020)
12. Jin, W. et al. Advancements in Dry Electrode Technologies: Towards Sustainable and Efficient Battery Manufacturing. *ChemElectroChem*, e202400288 (2024)
13. Lu, Y. et al. Dry electrode technology, the rising star in solid-state battery industrialization. *Matter* **5**, 876–898 (2022).
14. Wei, Z. et al. Removing electrochemical constraints on polytetrafluoroethylene as dry-process binder for high-loading graphite anodes. *Joule* **8**, 1350–1363 (2024).
15. Liu, Y. et al. Roll-to-roll solvent-free manufactured electrodes for fast-charging batteries. *Joule* **7**, 952–970 (2023).
16. Kwon, K. et al. Low-Resistance $LiFePO_4$ Thick Film Electrode Processed with Dry Electrode Technology for High-Energy-Density Lithium-Ion Batteries. *Small Sci.* **4**, 2300302 (2024)

17. Kim, J. et al. 10 mAh cm^{-2} Cathode by Roll-to-Roll Process for Low Cost and High Energy Density Li-Ion Batteries. *Adv. Energy Mater.* **14**, 2303455 (2024).
18. Lee, D. et al. Shear force effect of the dry process on cathode contact coverage in all-solid-state batteries. *Nat. Commun.* **15**, 4763 (2024).
19. Buck, R. C. et al. Perfluoroalkyl and polyfluoroalkyl substances in the environment: Terminology, classification, and origins. *Integr. Environ. Assess. Manag.* **7**, 513–541 (2011).
20. Puts, G. J., Crouse, P. & Ameduri, B. M. Polytetrafluoroethylene: Synthesis and Characterization of the Original Extreme Polymer. *Chem. Rev.* **119**, 1763–1805 (2019).
21. Huber, S., Moe, M. K., Schmidbauer, N., Hansen, G. & Herzke, D. Emissions from incineration of fluoropolymer materials. *A literature survey. Kjeller: Norwegian Institute for Air Research*, 58 (2009).
22. The Danish Environmental Protection Agency, *Survey of selected fluorinated greenhouse gases*, https://mst.dk/publikationer/2014/december/survey-of-selected-fluorinated-greenhouse-gases (2015)
23. Purohit, P. & Höglund-Isaksson, L. Global emissions of fluorinated greenhouse gases 2005–2050 with abatement potentials and costs. *Atmos. Chem. Phys.* **17**, 2795–2816 (2017).
24. European Chemical Agency, *ECHA publishes PFAS restriction proposal*, https://echa.europa.eu/-/echa-publishes-pfas-restriction-proposal, (2023)
25. Glüge, J. et al. An overview of the uses of per- and polyfluoroalkyl substances (PFAS). *Environ. Sci.: Process. Impacts* **22**, 2345–2373 (2020).
26. Lohmann, R. et al. Are Fluoropolymers Really of Low Concern for Human and Environmental Health and Separate from Other PFAS?. *Environ. Sci. Technol.* **54**, 12820–12828 (2020).
27. Sajid, M. & Ilyas, M. PTFE-coated non-stick cookware and toxicity concerns: a perspective. *Environ. Sci. Pollut. Res.* **24**, 23436–23440 (2017).
28. Andreatta, F. et al. Degradation of PTFE non-stick coatings for application in the food service industry. *Eng. Fail. Anal.* **115**, 104652 (2020).
29. Akinci, A. & Cobanoglu, E. Coating of Al mould surfaces with polytetrafluoroethylene (PTFE), fluorinated ethylene propylene (FEP), perfluoroalkoxy (PFA) and ethylene-tetrafluoroethylene (ETFE). *e-Polymers* **9** (2009)
30. Diehm, R. et al. High-Speed Coating of Primer Layer for Li-Ion Battery Electrodes by Using Slot-Die Coating. *Energy Technol.* **8**, 2000259 (2020).
31. Zhang, Y. et al. Revisiting polytetrafluorethylene binder for solvent-free lithium-ion battery anode fabrication. *Batteries* **8**, 57 (2022).
32. Wu, Q., Zheng, J. P., Hendrickson, M. & Plichta, E. J. Dry process for fabricating low cost and high performance electrode for energy storage devices. *MRS Adv.* **4**, 857–863 (2019).
33. Li, G., Xue, R. & Chen, L. The influence of polytetrafluorethylene reduction on the capacity loss of the carbon anode for lithium ion batteries. *Solid State Ion.* **90**, 221–225 (1996).
34. Han, S. et al. Mitigating PTFE decomposition in ultra thick dry-processed anodes for high energy density lithium-ion batteries. *J. Energy Storage* **96**, 112693 (2024).
35. Suh, Y., Koo, J. K., Im, H. -j & Kim, Y.-J. Astonishing performance improvements of dry-film graphite anode for reliable lithium-ion batteries. *Chem. Eng. J.* **476**, 146299 (2023).
36. Sudhakaran, S. & Bijoy, T. A comprehensive review of current and emerging binder technologies for energy storage applications. *ACS Appl. Energy Mater.* **6**, 11773–11794 (2023).
37. Tao, R. et al. Unraveling the impact of the degree of dry mixing on dry-processed lithium-ion battery electrodes. *J. Power Sources* **580**, 233379 (2023).
38. Yang, C.-J., Leveen, L. & King, K. Ethane as a Cleaner Transportation Fuel. *Environ. Sci. Technol.* **49**, 3263–3264 (2015).
39. Sotomayor, M. E. et al. Ultra-thick battery electrodes for high gravimetric and volumetric energy density Li-ion batteries. *J. Power Sources* **437**, 226923 (2019).
40. Sun, X. et al. Enhancing the Performance of PVDF/GO Ultrafiltration Membrane via Improving the Dispersion of GO with Homogeniser. *Membranes* **12**, 1268 (2022).
41. Xie, Y. et al. Paraffin/polyethylene/graphite composite phase change materials with enhanced thermal conductivity and leakage-proof. *Adv. Compos. Hybrid. Mater.* **4**, 543–551 (2021).
42. Yoon, H. et al. Review of the Mechanistic and Structural Assessment of Binders in Electrodes for Lithium-Ion Batteries. *Int. J. Energy Res.* **2024**, 8893580 (2024).
43. Lee, K., Jo, Y., Nam, J. S., Yu, H. & Kim, Y.-J. Dry-film technology employing cryo-pulverized polytetrafluoroethylene binder for all-solid-state batteries. *Chem. Eng. J.* **487**, 150221 (2024).
44. Son, B. et al. Measurement and analysis of adhesion property of lithium-ion battery electrodes with SAICAS. *ACS Appl. Mater. interfaces* **6**, 526–531 (2014).
45. Oberacker, R. Powder compaction by dry pressing. *Ceram. Sci. Technol.* **3**, 3–37 (2012).
46. Ryu, M., Hong, Y.-K., Lee, S.-Y. & Park, J. H. Ultrahigh loading dry-process for solvent-free lithium-ion battery electrode fabrication. *Nat. Commun.* **14**, 1316 (2023).
47. Améduri, B. & Hori, H. J. C. S. R. Recycling and the end of life assessment of fluoropolymers: recent developments, challenges and future trends. *Chem. Soc. Rev.* **52**, 4208–4247 (2023).
48. Ajeti, A. D. & Vyas, S. J. C. E. J. A. Gas phase product evolution during high temperature pyrolysis of PTFE: Development of ReaxFF simulation protocol. *Chem. Eng. J. Adv.* **19**, 100622 (2024).
49. Son, Y. et al. Analysis of differences in electrochemical performance between coin and pouch cells for lithium-ion battery applications. *Energy Environ. Mater.* **7**, e12615 (2024).
50. Chouchane, M., Yao, W., Cronk, A., Zhang, M. & Meng, Y. S. Improved Rate Capability for Dry Thick Electrodes through Finite Elements Method and Machine Learning Coupling. *ACS Energy Lett.* **9**, 1480–1486 (2024).
51. Liu, H. et al. An analytical model for the CC-CV charge of Li-ion batteries with application to degradation analysis. *J. Energy Storage* **29**, 101342 (2020).
52. Ning, G., White, R. E. & Popov, B. N. A generalized cycle life model of rechargeable Li-ion batteries. *Electrochim. Acta* **51**, 2012–2022 (2006).
53. Azmi, R. et al. An XPS study of electrolytes for Li-ion batteries in full cell LNMO vs Si/graphite. *ACS Appl. Mater. Interfaces* **16**, 34266–34280 (2024).
54. Tao, R. et al. Insights into the chemistry of the cathodic electrolyte interphase for PTFE-based dry-processed cathodes. *ACS Appl. Mater. Interfaces* **15**, 40488–40495 (2023).
55. Oh, H. et al. Development of a feasible and scalable manufacturing method for PTFE-based solvent-free lithium-ion battery electrodes. *Chem. Eng. J.* **491**, 151957 (2024).
56. Kresse, G. & Furthmüller, J. Efficient iterative schemes for ab initio total-energy calculations using a plane-wave basis set. *Phys. Rev. B* **54**, 11169–11186 (1996).
57. Kresse, G. & Furthmüller, J. Efficiency of ab-initio total energy calculations for metals and semiconductors using a plane-wave basis set. *Comput. Mater. Sci.* **6**, 15–50 (1996).
58. Kresse, G. Ab initio molecular dynamics for liquid metals. *J. Non-Crystalline Solids* **192-193**, 222–229 (1995).
59. Grimme, S. Semiempirical GGA-type density functional constructed with a long-range dispersion correction. *J. Comput. Chem.* **27**, 1787–1799 (2006).

60. Schmidt, M. W. et al. General atomic and molecular electronic structure system. *J. Comput. Chem.* **14**, 1347–1363 (1993).
61. Lee, C., Yang, W. & Parr, R. G. Development of the Colle-Salvetti correlation-energy formula into a functional of the electron density. *Phys. Rev. B* **37**, 785–789 (1988).
62. Becke, A. D. Density-functional thermochemistry. III. The role of exact exchange. *J. Chem. Phys.* **98**, 5648–5652 (1993).

Acknowledgements

This research was supported by a National Research Council of Science & Technology (NST) grant by the Korea government (MSIT) (No. CAP 21045-000, No. GTL24011-000) and the DGIST Start-up Fund Program of the Ministry of Science and ICT(2025020005).

Author contributions

Min Kyung Kim, Taegyun Yu, Sungbin Jang, Jinsoo Kim are responsible for the experimental design and manuscript preparation. Min Kyung Kim, Taegyun Yu, Sungbin Jang, Juho Lee, Hyeseong Oh, Min Jang, Hyungyeon Cha., Seung Min Lee, Hyeongseok Shim, Kwon-Hyung Lee performed most of the experiments and characterizations. Huiyeol Lee, Joonhee Kang. carried out DFT calculations. Gyujin Song, Wooyoung Jin, Tae-Hee Kim, Sinho Choi, Kyeong-Min Jeong, Joong Tark Han, Jung-Keun Yoo, Hun-Gi Jung assisted with the experimental details and the discussions. Sanghyun Song, Myoungkeon Park, Jinwoo Seong, Dongoh Kim provided technical advice for optimizing paraffin-based dry electrode manufacturing. Hyunwoo Choi, Minjong Seong, Min Jin Lim, Wook Ryol Hwang performed continuous twin-screw based dry mixing. Jieun Nam, Sanghoon Jo contributed to the 3D reconstruction of dry electrodes. Jinsoo Kim conceived the research idea and supervised the project.

Competing interests

Jinsoo Kim is named as an inventor on application of PCT (PCT/KR2024/017344) and patent of Republic of Korea (10-2024-0067630, 10-2024-0074946) filed by Korea Institute of Energy Research that covers these and related classes of paraffin-based dry electrode binders, as well as aspects of their use in electrochemical devices. The remaining authors declare no competing interests.

Additional information

Supplementary information The online version contains supplementary material available at https://doi.org/10.1038/s41467-025-66082-3.

Correspondence and requests for materials should be addressed to Jinsoo Kim.

Peer review information *Nature Communications* thanks Qiang Zhang, Arthur Dupuy, Zheng Chen and the other, anonymous, reviewer(s) for their contribution to the peer review of this work. A peer review file is available.

[1]Ulsan Advanced Energy Technology R&D Center, Korea Institute of Energy Research, Ulsan, Republic of Korea. [2]Department of Nano Fusion Technology, Pusan National University, Busan, Republic of Korea. [3]Department of Energy Science and Engineering, Daegu Gyeongbuk Institute of Science and Technology (DGIST), Daegu, Republic of Korea. [4]Department of Organic Material Science and Engineering, Pusan National University, Busan, Republic of Korea. [5]Department of Energy Engineering, School of Energy and Chemical Engineering, Ulsan National Institute of Science and Technology (UNIST), Ulsan, Republic of Korea. [6]School of Chemical Engineering, University of Ulsan, Ulsan, Republic of Korea. [7]Nano Hybrid Technology Research Center, Creative and Fundamental Research Division, Korea Electrotechnology Research Institute (KERI), Changwon, Republic of Korea. [8]Department of Electro-Functionality Materials Engineering, University of Science and Technology (UST), Changwon, Republic of Korea. [9]Energy Storage Research Center, Korea Institute of Science and Technology (KIST), Seoul, Republic of Korea. [10]Division of Energy and Environment Technology, KIST School, University of Science and Technology, Seoul, Republic of Korea. [11]Department of Energy Science, Sungkyunkwan University, Suwon, Republic of Korea. [12]KIST-SKKU Carbon-Neutral Research Center, Sungkyunkwan University, Suwon, Republic of Korea. [13]R&D Center, Rechargeable Battery Division, Hanwha Momentum, Seongnam, Republic of Korea. [14]School of Mechanical Engineering, Gyeongsang National University, Jinju, Republic of Korea. [15]R&D Center, Yunsung F&C Co., Ltd., Anseong, Republic of Korea. [16]Multiphysics Digital Twin Lab, Trinity Engineering, Seoul, Republic of Korea. [17]These authors contributed equally: Min Kyung Kim, Taegyun Yu, Sungbin Jang. ✉e-mail: jinsoo.kim@dgist.ac.kr